



Reduction of FeO/Pt(1 1 1) thin films by exposure to atomic hydrogen

Jan Knudsen^a, Lindsay R. Merte^a, Lars C. Grabow^b, Falk M. Eichhorn^b, Soeren Porsgaard^a, Helene Zeuthen^a, Ronnie T. Vang^a, Erik Lægsgaard^a, Manos Mavrikakis^b, Flemming Besenbacher^{a,*}

^aInterdisciplinary Nanoscience Center (iNANO), Department of Physics and Astronomy, Aarhus University, DK-8000 Aarhus C, Denmark

^bDepartment of Chemical and Biological Engineering, University of Wisconsin-Madison, Madison, WI 53706, USA

ARTICLE INFO

Article history:

Received 22 September 2009

Accepted for publication 8 October 2009

Available online 14 October 2009

Keywords:

Iron-oxide film

Reduction

Scanning tunneling microscopy

Water

Metal-oxide

X-ray photoelectron spectroscopy

ABSTRACT

Using scanning tunneling microscopy (STM), X-ray photoemission spectroscopy (XPS) and density functional theory (DFT) calculations we have studied the reduction of ultra-thin films of FeO(1 1 1) grown on Pt(1 1 1) after exposure to atomic hydrogen at room temperature. A number of new ordered, partly-reduced FeO_x structures are identified and as a general trend we reveal that all the reduced FeO_x structures incorporate 2-fold coordinated Fe atoms as opposed to the original 3-fold coordinated Fe atoms in the FeO film. We find that when all the Fe atoms are 2-fold O-coordinated the FeO_x surface structure is resistant to further reduction at room temperature. We observe that water easily dissociates on the most heavily reduced FeO_x structure in contrast to the initially inert FeO film, and reveal that it is possible to partially re-oxidize the FeO_x film by heating the surface slightly in the presence of water.

© 2009 Elsevier B.V. All rights reserved.

1. Introduction

Numerous studies have demonstrated that ultra-thin oxides exhibit novel physical and chemical properties compared to their bulk counterparts. In particular, reducible metal oxides grown on noble metal surfaces have been shown to form a variety of phases having structures and stoichiometries with no known bulk analogues, resulting from both two-dimensional confinement and electronic interactions with the substrate [1,2]. Netzer has noted the general tendency of transition metals to stabilize ultra-thin oxides in lower oxidation states compared to bulk phases [3], an effect which has significant implications for heterogeneous catalysis and the reactivity of transition metal oxides.

Such effects may be important for FeO_x/Pt catalysts, which have been found to be active for selective CO oxidation in hydrogen [4,5], the oxygen reduction reaction [6], and the water–gas shift reaction [7,8]. Qin et al. [9] have shown that platinum nanoparticles on Fe₃O₄ become encapsulated by a thin layer of FeO when exposed to reducing conditions, a phenomenon that has been implicated in the strong metal-support interaction. Huang and Ranke [10] studied the reduction of a 1 ML FeO film on Pt(1 1 1) by atomic hydrogen and identified a substoichiometric FeO_x phase that wets the surface and is resistant to further reduction. Whereas metallic platinum is observed to stabilize iron oxides in low oxidation states one would expect Pt to destabilize oxides in higher oxidation states, effectively making them more reactive oxidants, and

experiments appear to confirm this. For example, electrochemical measurements by Wang et al. [11] have shown that a charge transfer from Fe₃O₄ to Pt enhances the reducibility of the oxide and alters the chemical properties of the metal. Apparently for similar reasons, an ultra-thin, oxygen-rich FeO_x film on Pt(1 1 1) was found to be a highly effective catalyst for CO oxidation [12]. Clearly, to attain a complete understanding of the interactions between iron oxides and platinum, atomic-scale characterization of the structures and chemical properties of FeO_x/Pt interfaces is highly desirable.

Here, we make use of high-resolution scanning tunneling microscopy (STM) and X-ray photoelectron spectroscopy (XPS) in combination with density functional theory (DFT) calculations to study the reduction of the 1 ML FeO film on Pt(1 1 1) by atomic hydrogen. The pristine film has been well-characterized in the past using STM [13,14], low-energy electron diffraction (LEED) and X-ray photoelectron diffraction [15], and its atomic structure is depicted in Fig. 1a. It consists of a hexagonal Fe-lattice sandwiched in between the Pt(1 1 1) substrate and a hexagonal surface layer of O atoms. The lattice mismatch between the hexagonal Fe/O-lattice (3.1 Å) and the Pt(1 1 1) substrate (2.78 Å) as well as a small rotation of the Fe/O-lattice relative to the substrate (~0.6°) leads to a characteristic moiré structure with ~25 Å periodicity, exhibiting a floreted pattern in LEED (Fig. 1b), and clearly discernible supercell in STM measurements (Fig. 1c). When the FeO surface structure is exposed to atomic hydrogen, oxygen is removed, desorbing as H₂O [10]. The O:Fe ratio of the film decreases steadily from 1 to ~0.65, and correspondingly we observe formation of several new FeO_x structures, beginning with vacancy dislocation

* Corresponding author. Tel.: +45 8942 3604/3711; fax: +45 8612 0740.
E-mail address: fbe@inano.dk (F. Besenbacher).

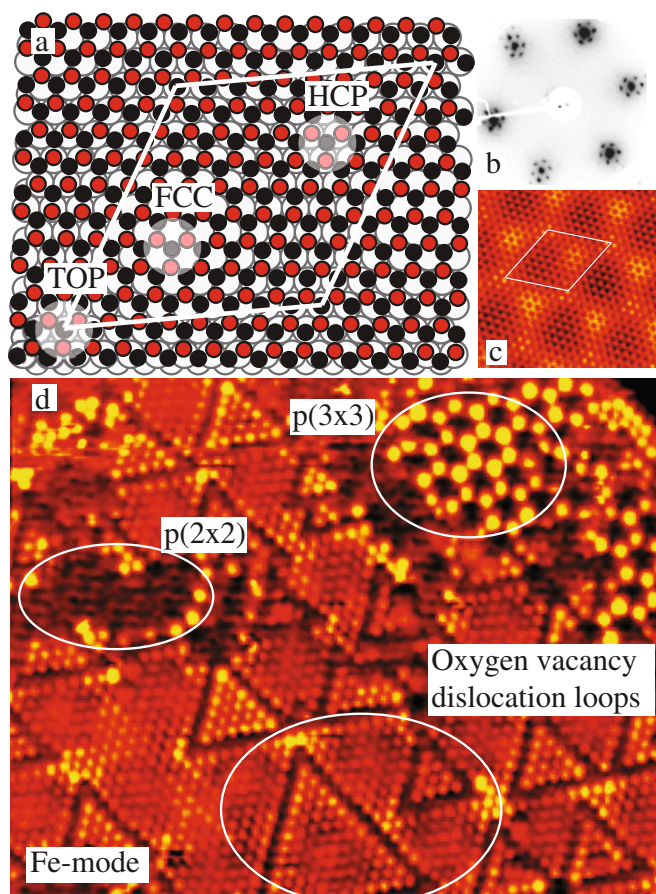


Fig. 1. (a) Atomic structure of the FeO(1 1 1) film with the three high-symmetry domains highlighted. Pt (white), Fe (black), and O (red). (b) 53.9 eV LEED image of the 1 ML FeO film, showing the characteristic floret pattern due to the film's moiré structure. (c) STM image ($60 \times 60 \text{ \AA}^2$, 3 nA, 65 mV) of the 1 ML FeO film, with the unit cell from (a) marked. (d) STM image ($150 \times 120 \text{ \AA}^2$, 1.76 nA, 55 mV) obtained after exposure of 9×10^{-6} mbar s atomic hydrogen and subsequent flashing to 450 K. Three different reduced structures are observed to coexist on the surface. Distinct protrusions correspond to 3-fold coordinated Fe atoms. (For interpretation of the references to colour in this figure legend, the reader is referred to the web version of this article.)

loops, which we have previously described briefly [16], followed by an ordered $p(3 \times 3)$ structure of stoichiometry Fe_4O_3 and finally a $p(2 \times 2)$ structure of stoichiometry Fe_3O_2 , which is resistant to further reduction. In Fig. 1d, an STM image is depicted showing the surface in an intermediate state of reduction, where these three structures are observed to coexist. Additionally, we have studied the interaction of water with the dislocation loop structure and with the Fe_3O_2 structure. The dislocation loops are found to be inert toward water dissociation under the present experimental conditions, similar to the case reported for the pristine FeO film [17,18], whereas water is found to dissociate reversibly on the Fe_3O_2 structure at room temperature and irreversibly at higher temperatures, partially re-oxidizing the FeO_x film.

2. Experimental and computational methods

STM measurements were carried out at room temperature with a home-built Aarhus-STM [19] mounted in an ultra-high vacuum (UHV) chamber with base pressure $\sim 1 \times 10^{-10}$ mbar. The Pt(1 1 1) crystal was cleaned by cycles of Ar^+ sputtering and subsequent annealing at 1000 K until it was clean as judged from atomically-resolved STM images. The FeO films were grown by cycles of Fe

deposition of submonolayer quantities at room temperature and subsequent oxidation at 870 K in 1.3×10^{-6} mbar O_2 for 2 min. It is straightforward to distinguish the FeO film from the Pt(1 1 1) substrate in the STM images, and because a layer-by-layer growth mode is observed up to 2.1 monolayers [14], the thickness of the FeO film can easily be controlled. One monolayer is here and in the remainder of this article defined as the iron and oxygen coverage in a perfect bilayer FeO film grown on Pt(1 1 1) (i.e. 0.8 ML with respect to the atom density of Pt(1 1 1)). The structure and cleanliness of the film were always checked with STM before experiments.

As molecular hydrogen does not react readily with the FeO film under UHV conditions [10,20], we used atomic hydrogen to study the reduction of the ultra-thin film. Atomic hydrogen was dosed with a commercial gas cracker (Oxford Applied Research TC-50) located approximately 10 cm from the sample. Before the cracker was turned on the H_2 pressure in the chamber was adjusted to the desired value. Fixed power settings of the cracker were used in all experiments (54 W) and the exposure time and pressure were used to vary the exposure. The cracker was always preheated for 30 s. before the sample was turned towards the H-beam to ensure a constant flux of atomic hydrogen during the entire exposure time. Exposures are calculated from the H_2 background pressure measured before the cracker was turned on. The actual exposure of H_{at} is unknown, but it is proportional to the dosing time with fixed H_2 pressure and cracker power settings. The flux of atomic hydrogen at the sample surface, for a given background H_2 pressure, is determined by the effective pumping speed of the chamber. The latter may vary for STM and XPS set-ups, but we estimate the flux to be approximately equal in both chambers.

To obtain more ordered structures and to desorb excess hydrogen we flashed the samples to ~ 500 K directly after exposure. Deionized, triply distilled water was filled in a small glass bulb and degassed by several freeze–pump–thaw cycles prior to use, and water exposures were performed by backfilling the UHV chamber.

The XPS measurements were performed at MAX-Lab, beam line I311, which is described in detail elsewhere [21]. All spectra were collected in normal emission with photon energies of 153 eV for Fe 3p, 380 eV for C 1s, 700 eV for O 1s, and 860 eV for Fe 2p. The spectra are normalized to the background and the binding energies are calibrated to the Fermi edge. The background due to the neighboring Pt 5p line was subtracted from all the Fe 3p spectra and a polynomial background was used for the O 1s spectra. Coverages of FeO_x and coverages of OH groups are calculated by fitting the O 1s spectra with two peaks with shape similar to the shape of pristine FeO. The coverage of the FeO film in the XPS experiments was calibrated by saturating the surface with CO at room temperature. Because CO only binds to the exposed Pt surface [22] the intensity of the C 1s signal can be used directly to follow the growth of the film. By cycles of Fe deposition (submonolayer amounts) at room temperature and subsequent oxidation, we tuned the coverage of FeO to the point where the C 1s signal disappeared. Furthermore we checked the status of the FeO film using LEED, which showed the expected primary 6-fold spots from the FeO film and a rosette pattern arising from the moiré structure [15].

Spin polarized density functional theory calculations using the DFT + U approach by Dudarev [23] with $U = 4$ eV and $J = 1$ eV [24] were performed using the VASP total energy code [25,26]. Similar to a previous study on this system, we used the projector augmented wave (PAW) method with a kinetic energy cutoff of 400 eV combined with the PW91 exchange–correlation functional [27] and chose anti-ferromagnetic initial guesses for the magnetic moment of Fe atoms [24]. The unit cells used in our calculations are consistent with the experimentally observed systems: a $\sqrt{91} \times \sqrt{91} \text{R}5.2^\circ$ unit cell with three layers of Pt atoms (Fe–Fe dis-

tance = 3.1 Å) was employed to estimate the energy gain for the formation of the small triangular dislocation loops and $p(2 \times 2)$ and $p(3 \times 3)$ unit cells with five layers of Pt atoms were used to study the $p(2 \times 2)$ and $p(3 \times 3)$ structures. For the $\sqrt{91} \times \sqrt{91}R5.2^\circ$ unit cell, the FeO film and the topmost layer of Pt were fully relaxed. For the $p(2 \times 2)$ and $p(3 \times 3)$ unit cells, the FeO film and top two Pt layers were fully relaxed. The Brillouin zone was sampled using the Gamma-point only for the $\sqrt{91} \times \sqrt{91}R5.2^\circ$ cells, a $6 \times 6 \times 1$ Monkhorst–Pack k-point grid for the $p(2 \times 2)$ unit cells and a $4 \times 4 \times 1$ Monkhorst–Pack k-point grid for the $p(3 \times 3)$ unit cells. All simulated STM images were generated in the Tersoff–Hamann approach with a sample bias of 65 mV and an electron isodensity of $1 \times 10^{-5} e/\text{Å}^3$.

3. Results and discussion

3.1. Oxygen vacancy dislocation loops

In a previous publication, we have described the atomic structure of the triangularly shaped features [16], observed at the onset of the reduction. In summary, they consist of oxygen vacancy dislocation loops with an edge length of either approximately 5 or 12 Fe atoms (incorporating 7 or 14 O vacancies, respectively). The smaller dislocation loops are always centered at HCP domains, while the larger dislocation loops are always centered at TOP domains. A schematic model of the atomic structures of both the large and small dislocation loops is shown Fig. 2b.

XPS measurements are consistent with this model of the triangular features, and almost identical O spectra obtained before and after mild reduction are shown in Fig. 2e. By comparison with STM experiments (to be discussed in more detail below, see Fig. 7b), we estimate that on this surface dislocation loops are found at 30–40% of the moiré unit cells, corresponding to a vacancy coverage of 3–4%. The O 1s spectrum shows no change in peak position and only a small decrease in intensity.

As has been reported for a number of different surface structures (see, for example, Refs. [28–30]), STM imaging of the FeO film is strongly dependent on the atomic-scale tip termination, leading to a number of imaging modes, where both the appearance of the high-symmetry domains of the moiré structure and the chemical species imaged are different. For example, under similar or identical current and bias conditions, STM images have been obtained showing Fe atoms, O atoms, or both simultaneously, and each of the high-symmetry domains has been imaged with the largest

apparent height. Tip changes are most often spontaneous, but can be induced by applying voltage pulses or by dipping the tip gently into the surface. The presence of dislocation loops on the surface allows these modes to be distinguished. STM images of two similar dislocation loops, which correspond to the smaller triangle depicted in Fig. 2b in different tip imaging modes are shown as Fig. 2c and d. Comparison of these images with the model reveals that Fig. 2c shows 3-fold coordinated Fe atoms as bright protrusions, while the 2-fold coordinated Fe atoms along the edge of the dislocation loops are invisible. The observation of a registry shift in Fig. 2d indicates that O atoms are imaged in this mode.

Inspection of Fig. 2b reveals that each of the small dislocation loops converts one HCP domain to an FCC* (where * indicates the opposite orientation with respect to the substrate, see Fig. 2a) domain by shifting the oxygen lattice, whereas each of the large dislocation loops converts three HCP domains to FCC* domains and one TOP domain to one TOP* domain. As we have previously reported, DFT calculations using pseudomorphic $P(2 \times 2)$ unit cells indicate that FCC-type domains are more stable by 0.1–0.2 eV per FeO unit compared to HCP-type domains, suggesting that the dislocation loops form as a result of the lattice mismatch, analogous to misfit dislocation loops observed in metal-on-metal growth [31]. Thus, each small dislocation loop stabilizes a single HCP domain, while each large dislocation loop stabilizes the three HCP domains at its corners (the TOP and TOP* domains are nearly isoenergetic).

Here, we present additional DFT calculations using the experimentally observed $\sqrt{91} \times \sqrt{91}R5.2^\circ$ unit cell to obtain further atomic-scale insight than was possible with the pseudomorphic $p(2 \times 2)$ unit cells. In these more elaborate DFT calculations, we investigate the formation of triangular dislocation loops from seven adjacent oxygen vacancies in both the FCC (converted to HCP*) and HCP (converted to FCC*) domains. For the HCP domain, formation of the dislocation loop structure results in an energy gain of 4.15 eV, while for the FCC domain, an energy gain of 0.53 eV is obtained. The difference of 3.62 eV between the two structures clearly explains the experimental observation that the smaller dislocation loops are always centered at HCP domains. Interestingly, however, the formation of a dislocation loop at an FCC domain is still slightly exothermic, despite the fact that the HCP* stacking configuration is less stable. This indicates that the dominant component of the energy gain is related to the structure of the dislocation loop itself, independent of the local stacking configuration, and suggests that these dislocation loops would form

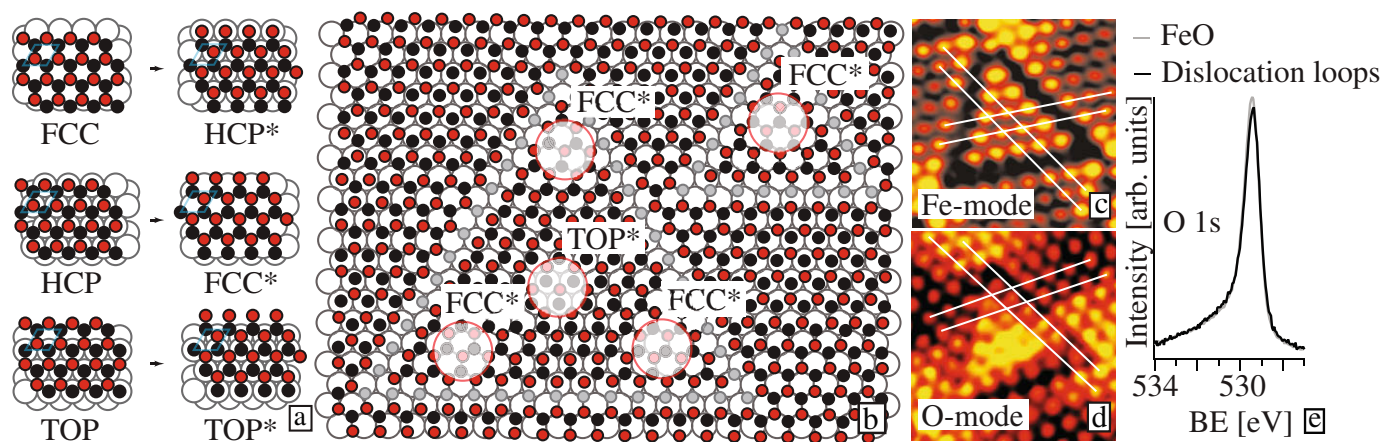


Fig. 2. (a) Illustration of the change in local stacking of the FeO film upon shifting the O lattice. The six different high-symmetry domains are shown, together with the nomenclature used in this work. (b) Atomic model of both the big and small dislocation loops. Pt (white), 3-fold Fe (black), 2-fold Fe (grey), and O (red). (c) Fe-mode STM image ($30 \times 30 \text{ Å}^2$, 1.04 nA, 19.5 mV) of a small dislocation loop. (d) O-mode STM image ($30 \times 30 \text{ Å}^2$, 0.52 nA, 6.4 mV) of a small dislocation loop. (e) O 1s XP-spectra of the pristine FeO film (grey) and the dislocation structure (black) obtained after exposure of 1.2×10^{-6} mbar s atomic hydrogen and subsequent flashing to 500 K. (For interpretation of the references to colour in this figure legend, the reader is referred to the web version of this article.)

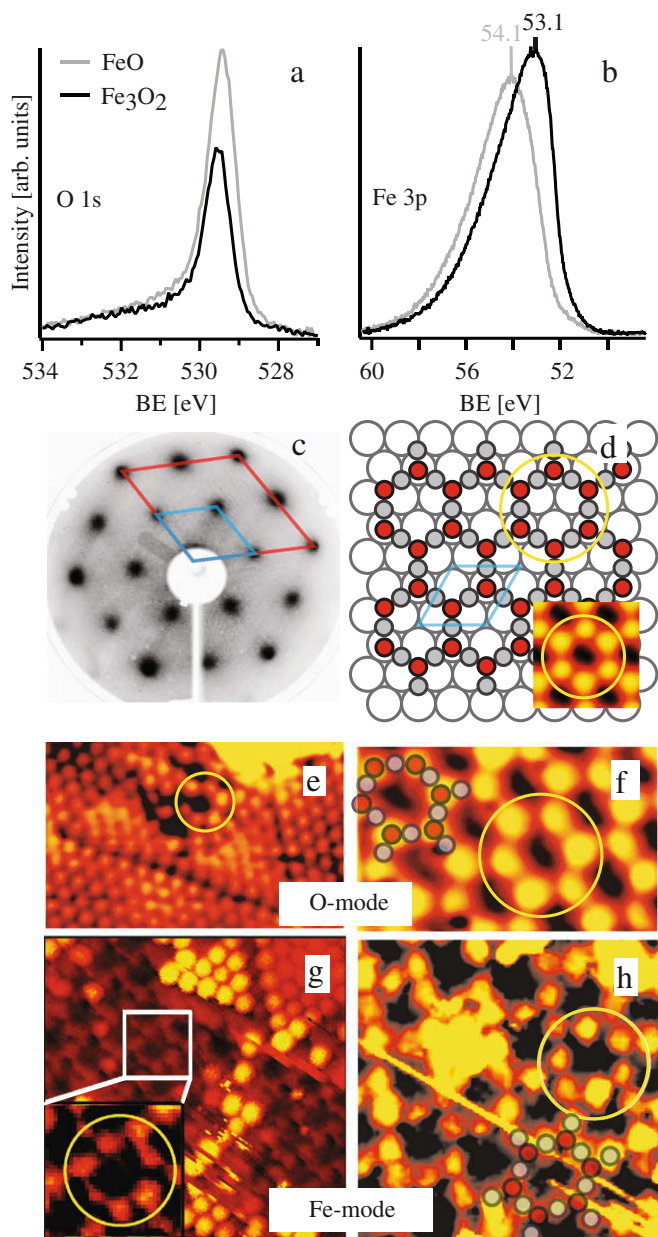


Fig. 3. (a) O 1s and (b) Fe 3p XP-spectra of the pristine FeO film (grey) and the $p(2 \times 2)$ structure (black). (c) 100 eV LEED image of the $p(2 \times 2)$ structure. The substrate unit cell is indicated in red, and the overlayer unit cell in blue. (d) Ball model of the proposed Fe_3O_2 structure. Inset: Tersoff–Hamann simulated STM image of the structure. (e) O-mode STM image of the mildly-reduced FeO film, showing dislocation loops and the oxygen honeycomb structure. (f) STM image of the $p(2 \times 2)$ structure showing a honeycomb pattern similar to (e). (g) Fe-mode STM image showing the edge of a dislocation loop (top) and the $p(2 \times 2)$ structure (middle). Inset: Excerpt with high contrast, showing the kagomé lattice of Fe atoms. (h) Fe-mode STM image of the $p(2 \times 2)$ structure showing the kagomé lattice of Fe atoms. (For interpretation of the references to colour in this figure legend, the reader is referred to the web version of this article.)

upon oxygen removal even in the absence of any lattice mismatch-related variation in overlayer-substrate bond strength.

3.2. The $p(2 \times 2)$ – Fe_3O_2 structure

Upon extensive exposure to atomic hydrogen at room temperature the FeO film is transformed completely into the $p(2 \times 2)$ structure, as revealed both in LEED and STM measurements. Typical experimental parameters used to prepare a uniform, locally well-ordered $p(2 \times 2)$ structure were 10 min. atomic hydrogen exposure

at 1.0×10^{-7} mbar H_2 background pressure at room temperature and subsequent flashing to 500 K to desorb any excess hydrogen.

The O 1s spectra obtained before and after reduction are depicted in Fig. 3a, and show a reduction in intensity of the oxygen signal by $\sim 33\%$, and only a small (+0.1 eV) shift in binding energy. Corresponding Fe 3p spectra are shown in Fig. 3b, and show a small increase in intensity following reduction, most likely due to a reduction in screening by the O layer, and a shift of 1.0 eV to lower binding energy. The LEED pattern obtained on this surface is shown in Fig. 3c and displays distinct, albeit somewhat diffuse, $p(2 \times 2)$ reflexes, indicative of relatively small coherent domains, consistent with STM and with previous observations [10].

The STM image in Fig. 1d, which depicts the partially-reduced FeO film imaged with an STM tip in the Fe-mode, shows similar contrast on the 2-fold coordinated Fe atoms along the edges of the dislocation loops and on the $p(2 \times 2)$ domains. This suggests that all Fe atoms in the $p(2 \times 2)$ structure are 2-fold coordinated to O atoms. Based on this observation, together with the results of XPS measurements, we propose the structural model depicted in Fig. 3d, which consists of a honeycomb lattice of O atoms superimposed on a kagomé lattice of Fe atoms. Each O atom is coordinated to three Fe atoms, while each Fe atom is coordinated to two O atoms, corresponding to a stoichiometry of Fe_3O_2 , consistent with the $\sim 1.5:1$ Fe:O ratio as estimated from XPS results.

As is the case for the pristine, unreduced FeO film, the Fe and O sublattices of the $p(2 \times 2)$ structure can be resolved separately in different tip-dependent STM imaging modes, as shown in Fig. 3f and h, and the protrusions in these STM images directly reveal the expected honeycomb and kagomé lattices, respectively. That the former corresponds to the oxygen lattice and the latter to the iron lattice is supported by STM images obtained on the more mildly-reduced FeO films, where domains of the $p(2 \times 2)$ structure coexist with the dislocation loop structure. In Fig. 3e an STM image is depicted where a small patch of the honeycomb structure is found to co-exist adjacent to two dislocation loops. The protrusions observed at these dislocation loops are out of registry with the protrusions for the surrounding FeO film, which is indicative of an O-specific STM tip imaging mode. Likewise, Fig. 3g shows a domain of the $p(2 \times 2)$ structure adjacent to the dislocation loops in the Fe-specific imaging mode. The apparent height of the $p(2 \times 2)$ structure is similar to that observed along the edges of the dislocation loop structure, and although the corrugation is very weak, a kagomé lattice of protrusions can be discerned, which is evident from the higher contrast image inset in Fig. 3g.

Since we know from DFT calculations that the FCC and HCP domains are more stable as compared to the TOP domains in the moiré-structured FeO film [16], we propose that Fe atoms occupy hollow sites on the Pt(1 1 1) surface, with one half of the oxygen atoms located at hollow sites and the other half in atop-Pt sites. For this model of the $p(2 \times 2)$ structure we can derive Fe- and O-coverages of 0.94 ML and 0.63 ML, respectively, with respect to the coverages of the FeO film. The slightly reduced coverage of Fe in the $p(2 \times 2)$ structure with respect to the pristine FeO film is likely compensated by a number of different defects which are always observed in the STM images of the $p(2 \times 2)$ structure.

To gain further confirmation of the Fe_3O_2 surface structure, we have carried out a detailed DFT study of a variety of structures with different O and Fe coverages. The most stable structures are subsequently compared to the structure revealed from the STM results. DFT calculations confirm that the structure depicted in Fig. 3d, with Fe at hollow sites, is indeed the most stable $p(2 \times 2)$ structure, and in the inset we have shown a simulated STM image obtained from the DFT calculations of the local density of states (LDOS) using the Tersoff–Hamann model. Although such simulated STM images must be treated with caution considering our observation that the tip state may play a strong role in STM imaging, the sim-

ulated image is consistent with much of our experimental data, as seen by comparison with Fig. 3f.

We have also in the DFT calculations considered structural models with H or Pt atoms which are incorporated in the “pocket sites” of the honeycomb structure, which might also be consistent with experimental data. However, the DFT calculations indicate that the most stable adsorption site for hydrogen is atop oxygen on this structure, forming OH, which we do not observe with XPS, suggesting that hydrogen fully desorbs during the flash to 500 K, in agreement with previous temperature programmed desorption (TPD) measurements [10]. Our DFT calculations also predict that CO should adsorb strongly (~ 2 eV binding energy) to a Pt adatom in the pocket site, but only weakly (~ 0.6 eV binding energy) on the Fe_3O_2 structure. XPS measurements showed no signs of CO adsorption upon dosing at room temperature, and we thus rule out the presence of Pt adatoms in the structure.

3.3. The $p(3 \times 3) - \text{Fe}_4\text{O}_3$ structure

At intermediate exposures of atomic hydrogen a $p(3 \times 3)$ structure is observed, which is always found, in the STM images, to coexist with the dislocation loop and $p(2 \times 2)$ structures. A LEED pattern obtained for a film containing both $p(2 \times 2)$ and $p(3 \times 3)$ structures is depicted in Fig. 4c. Corresponding O 1s and Fe 3p spectra are shown in Fig. 4a and b, together with that of the unreduced, pristine FeO. The decrease in O 1s intensity is $\sim 25\%$ and the shift in the Fe 3p peak position is 0.7 eV to lower binding energy. These values, together with the fact that the $p(3 \times 3)$ structure can be removed and converted into the $p(2 \times 2)$ structure by further exposure to atomic hydrogen, suggest that this structure has an Fe:O ratio intermediate between that of the unreduced FeO and the Fe_3O_2 phase.

Again turning to the STM image depicted in Fig. 1d, we find that in the Fe imaging mode, the $p(3 \times 3)$ structure is imaged as a honeycomb of bright protrusions, which mark the positions of 3-fold coordinated Fe atoms. Furthermore, a number of STM images obtained of coexisting $p(2 \times 2)$ and $p(3 \times 3)$ domains show distinct similarity between the two structures, and both tend to show 6-fold symmetry. An example of this is depicted in Fig. 4d, where similar bright protrusions are observed in positions marked by blue ($p(2 \times 2)$) and green ($p(3 \times 3)$) hexagons. Taking these observations into account, the structural model shown in Fig. 4e can be constructed beginning with placement of the 3-fold coordinated Fe atoms in a $p(3 \times 3)$ unit cell, with three O atoms over hollow sites and three atop Pt, connected by 2-fold coordinated Fe atoms. An alternate model, shown in Fig. 4f, is formed by placing all O atoms over Pt-hollow sites. Both models have Fe_4O_3 stoichiometry with Fe- and O-coverages of 1.11 ML and 0.83 ML, respectively, relative to the coverages of the FeO film.

DFT calculations indicate that the structure depicted in Fig. 4e, with Fe at hcp hollow sites and O at fcc and atop sites, is the most stable one, being lower in energy by >1 eV than the structure depicted in Fig. 4f. Simulated STM images of this structure, shown as insets in Fig. 4e and f show protrusions over O atoms, as was the case for the $p(2 \times 2)$ structure. The STM image depicted in Fig. 4g shows an O-mode STM image of the $p(3 \times 3)$, $p(2 \times 2)$ and dislocation loop structures. The honeycomb lattice of the $p(2 \times 2)$ and the characteristic triangles of the $p(3 \times 3)$ structure can be clearly observed, in excellent agreement with DFT simulated STM images, which strongly support the structural models proposed.

3.4. Overview of the reduction process – XPS results

Having described the structures formed upon reduction of the FeO film by atomic hydrogen, we now examine the overall reduction process in further detail.

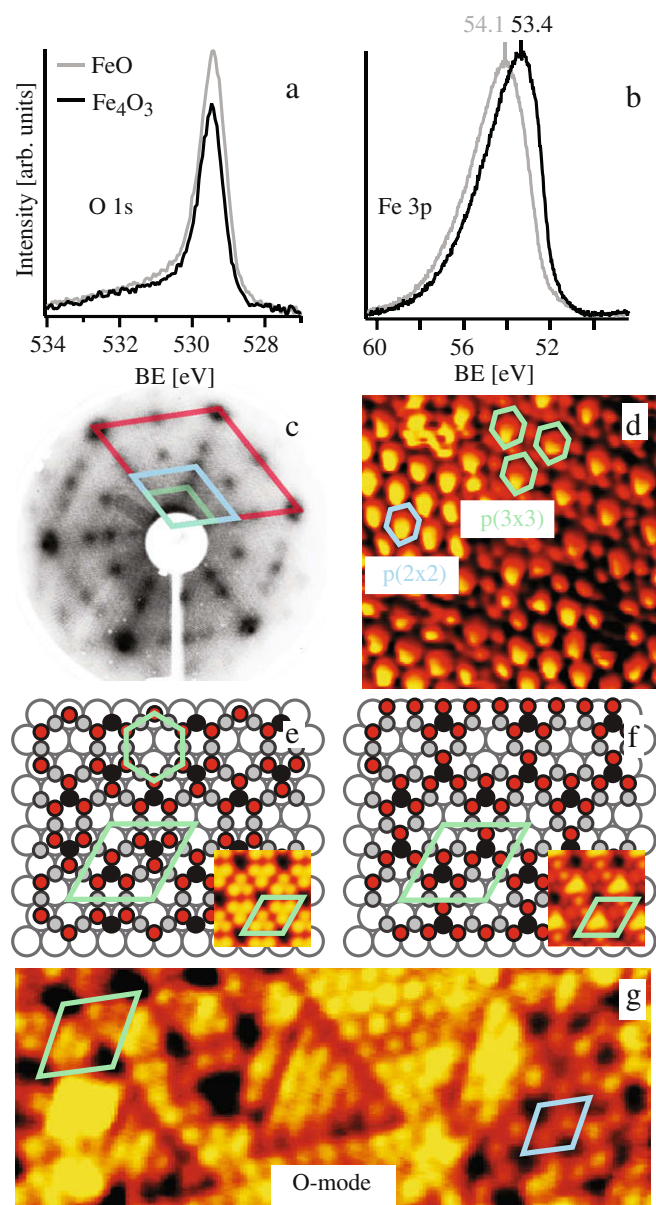


Fig. 4. (a) O 1s and (b) Fe 3p XP-spectra of the pristine FeO film (grey) and a partially-reduced FeO film exhibiting both $p(2 \times 2)$ and $p(3 \times 3)$ structures (black). (c) 100 eV LEED image of the surface corresponding to the XP-spectra. The Pt(1 1 1) unit cell is indicated in red, the $p(2 \times 2)$ unit cell in blue and the $p(3 \times 3)$ in green. (d) STM image showing coexisting $p(2 \times 2)$ (blue hexagon) and $p(3 \times 3)$ (green hexagons) phases. Note the similar bright protrusions and the 6-fold symmetry of both phases around these sites. (e and f) Structural models incorporating 3-fold coordinated Fe in the observed honeycomb pattern, with Tersoff–Hamann simulated STM images shown as insets. Structure (e) is more stable by ~ 1 eV. (g) Atomically-resolved STM image showing the $p(3 \times 3)$ (green unit cell), $p(2 \times 2)$ (blue unit cell) and dislocation loop structures in an O-specific STM tip mode. Note the good correspondence with simulated STM images of both the $p(2 \times 2)$ and $p(3 \times 3)$ structures. (For interpretation of the references to colour in this figure legend, the reader is referred to the web version of this article.)

Following exposure to atomic hydrogen, we observe by XPS the formation of hydroxyls on the surface, indicated by the appearance of an O 1s peak at 531.7 eV, shifted +2.2 eV relative to the main peak at 529.5 eV assigned to oxygen in FeO. A shift of +2.2 eV agrees well with the reported value for OH groups on $\alpha\text{-Fe}_2\text{O}_3(0001)$ [32,33]. O 1s spectra of the clean (a1) and hydroxylated FeO film (a2) are shown in Fig. 5a.

Spectrum (a2) in Fig. 5a clearly shows a peak at 531.7 eV corresponding to OH and a peak at 529.5 eV corresponding to FeO_x . The

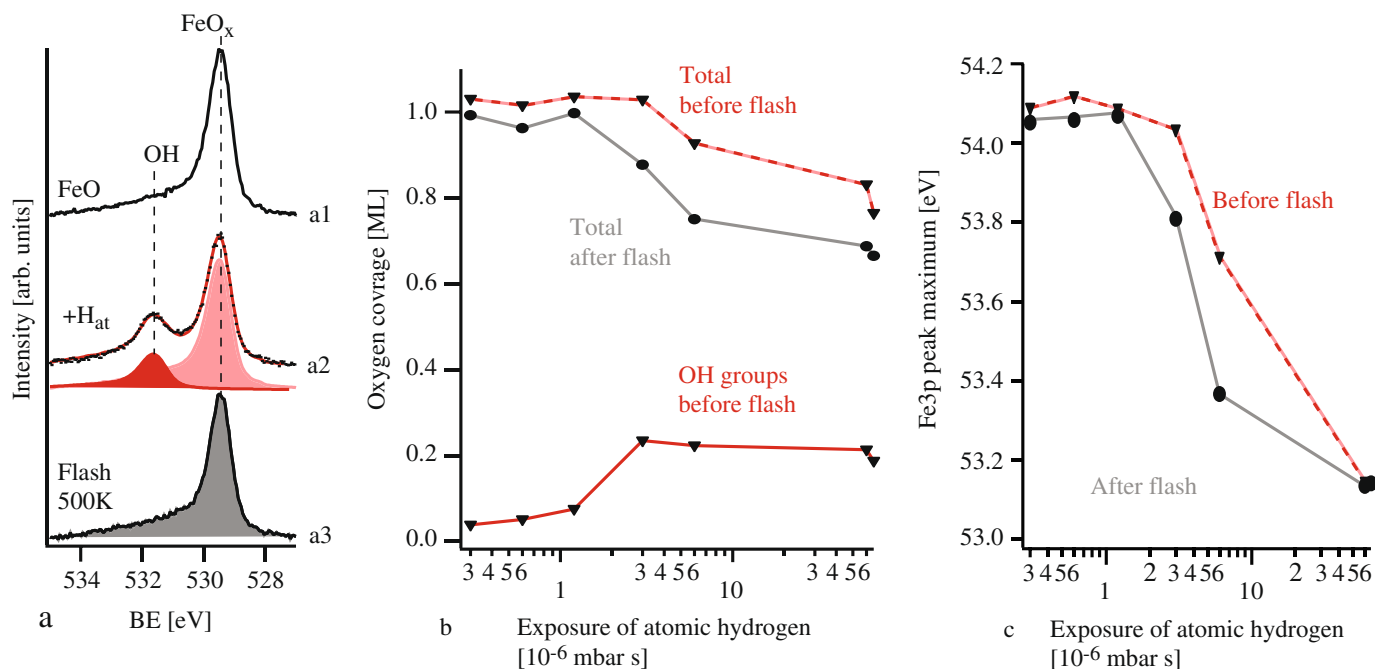


Fig. 5. (a) XPS-spectra of the O 1s region of the clean FeO film (a1), the FeO film exposed to 3×10^{-6} mbar s hydrogen (a2) and subsequently flashed to 500 K (a3). (b) Total oxygen coverage and coverage of OH groups calculated by fitting the O 1s spectra. The grey curve shows the oxygen coverage after the H-exposed surface was flashed to 500 K. (c) Fe 3p peak maxima as function of the exposure to atomic hydrogen for the exposed FeO films before (red) and after flashing to 500 K (grey). (For interpretation of the references to colour in this figure legend, the reader is referred to the web version of this article.)

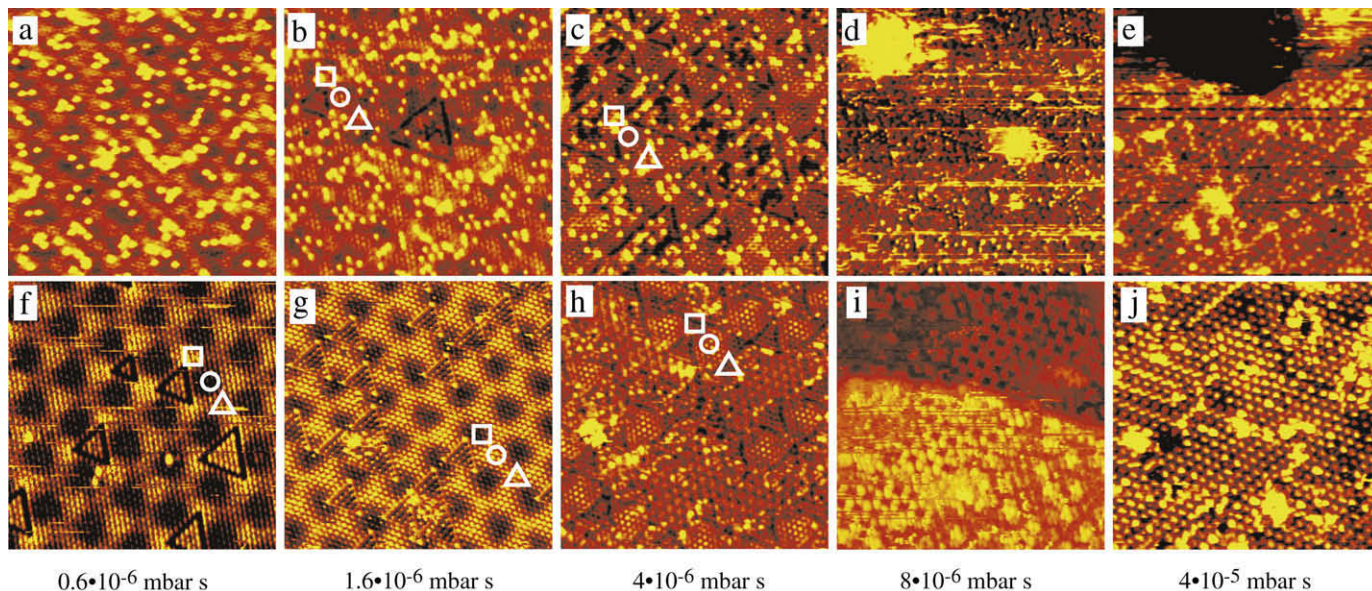


Fig. 6. (a–e) STM images ($140 \times 140 \text{ \AA}^2$) obtained directly after exposure to atomic hydrogen at room temperature. TOP, HCP and FCC domains are indicated with \circ , Δ , and \square , respectively, using the convention from Refs. [16,24]. Exposures are given in the figure. (f–j) Representative STM images ($140 \times 140 \text{ \AA}^2$) obtained after exposure and a subsequent flash to 500 K.

areas of the both peaks, referenced to the O 1s signal of the pristine FeO film, are measured as function of atomic hydrogen exposure and the total oxygen coverage and the coverage of OH groups are plotted in Fig. 5b. The XPS measurements show that the OH coverage increases with exposure to a maximum of 0.23 ML at 3×10^{-6} mbar s, after which it decreases to a limiting value of 0.19 ML following long atomic hydrogen exposure. Until the maximum OH coverage is reached, the total oxygen coverage is approximately unchanged, indicating that accumulation of hydrogen on the surface, without detectable oxygen removal, dominates in this

phase. At exposures above 3×10^{-6} mbar s, the total oxygen coverage start to decrease, indicating that significant removal of oxygen begins at this point.

After flashing the hydrogen-exposed FeO film to 500 K the O 1s peak assigned to OH groups disappears as Fig. 5a3 demonstrates. The energy of the O 1s peak assigned to FeO_x is unaffected, but a clear reduction of the intensity compared to the pristine FeO film is observed. Fig. 5b shows the reduction of the FeO_x peak, referenced to the O 1s signal of the pristine FeO film, after different exposures of hydrogen and a subsequent flash. In this case, no

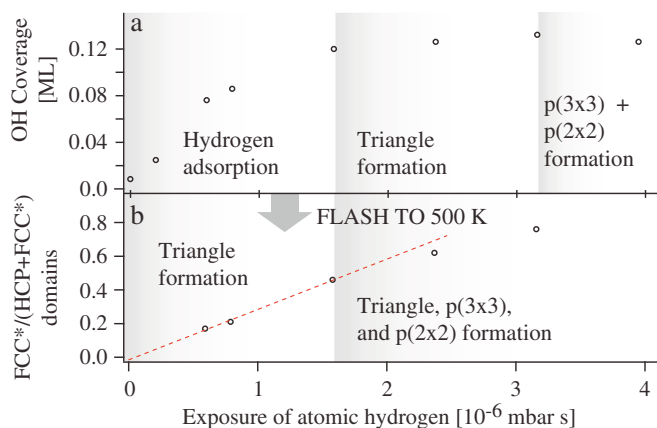


Fig. 7. (a) Coverage of OH groups calculated from the protrusion observed in STM images for different exposures of atomic hydrogen. (b) Relative number of HCP domains converted to FCC* domains after hydrogen adsorption and subsequent flashing to 500 K.

significant decrease in the O 1s signal can be detected for exposures up to 1.2×10^{-6} mbar s. Above this point, reduction in the O 1s signal becomes significant, and continues until an oxygen coverage of ~ 0.65 ML is reached after long exposure.

The Fe 3p core level in the FeO and the FeO_x structures can also be used to follow the details of the reduction process. Both the Fe 2p and Fe 3p peaks have complicated multiplet structures [34] and rather than deconvoluting into a large number of peaks we simply used the position of the peak maximum to follow the reduction of the FeO film. For the H-exposed and subsequently flashed FeO films (see Fig. 5c) we observe that the Fe 3p peak position begins to decrease rapidly above 1.2×10^{-6} mbar s from its initial position at 54.1 eV. After long exposure the Fe 3p peak position reaches a value of 53.1 eV, halfway between that of the pristine film and of metallic Fe deposited on Pt(1 1 1), for which we measure a Fe 3p peak position of 52.2 eV. Thus, the FeO film does not completely reduce to metallic Fe. Comparing the measurements obtained for reduction at room temperature and upon heating to 500 K, we observe that induction periods, prior to onset of the oxygen reduction, exist in both cases, and that the atomic hydrogen threshold exposure at room temperature ($\sim 3 \times 10^{-6}$ mbar s) is roughly double that observed when the sample is flashed to 500 K ($\sim 1.2 \times 10^{-6}$ mbar s).

Coincident with the reduction in O 1s intensity and the shift in Fe 3p binding energy, both $p(3 \times 3)$ and $p(2 \times 2)$ reflexes appear in the LEED patterns obtained following the XPS measurements (Figs. 3c and 4c). The ordered LEED patterns, together with the intermediate Fe 3p binding energy and presence of oxygen on the surface, indicate that ordered, partially-reduced structures are formed on the surface, in agreement with our STM results presented above and with previous results [10].

3.5. Overview of the reduction process – STM results

In order to gain further insight into the reduction of the FeO film, we have performed a detailed STM study of the evolution of FeO surface structure following exposure to atomic hydrogen and subsequent heating. An overview of selected STM images after different exposures is shown in Fig. 6a–e.

The hydroxyls formed initially on the surface upon atomic hydrogen exposure are clearly visible as bright protrusions in the STM images shown in Fig. 6a–c. We observe that the individual OH-related protrusions can be removed locally by applying tip voltage pulses ($U \geq 2.5$ V) during scanning; similar behavior has been observed previously for hydrogen adsorbed on an oxide

[35] and a metal surface [36]. Below an exposure of 1.6×10^{-6} mbar s, we observe that the coverage of hydroxyl groups increases steadily with the atomic hydrogen exposure (Fig. 7a), with no indications that oxygen is removed from the surface. Above this point, where the OH coverage deduced from STM images is 0.12 ML, the triangular oxygen vacancy dislocation loops begin to form, as shown in Fig. 6b. More extensive reduction of the FeO surface is observed above an exposure of $\sim 4 \times 10^{-6}$ mbar s, where dark pits are observed in STM images, as depicted in Fig. 6c. Atomically-resolved images of these pits have not been obtained, but they presumably correspond to small oxygen-depleted domains incorporating elements of the $p(2 \times 2)$ and $p(3 \times 3)$ structures. Thereafter, STM imaging becomes more difficult, with poor tip stability indicative of weakly-bound, mobile species on the surface. Nonetheless, the formation and eventual saturation of the surface by the $p(2 \times 2)$ phase at higher exposures can be seen in Fig. 6d and e.

Fig. 6f–j show STM images of each H-exposed surface after flashing to 500 K. Surface hydroxyls are removed during the temperature flash and the coverage of reduced structures is observed to increase, consistent with TPD measurements by Huang and Ranke showing that hydrogen desorbs from the surface both as H₂ and H₂O upon heating from 300 K to 500 K [10]. The structures observed after flashing show an even better ordering and as a result of this, as well as the much-improved tip stability following desorption of hydrogen, characterization of the surface with STM becomes much easier. As was the case during room-temperature exposure to H, the initial stage of reduction involves the formation of dislocation loops, and analysis of a large number of STM images indicates that their coverage increases approximately linearly with exposure up to $\sim 1.6 \times 10^{-6}$ mbar s (see Fig. 7b), at which point vacancy dislocation loops have converted half of the film's HCP domains to FCC* domains. At higher atomic hydrogen exposures, $p(2 \times 2)$ and $p(3 \times 3)$ structures are formed, covering increasing areas of the surface until finally the $p(2 \times 2)$ structure is the only phase observed, in excellent agreement with XPS and LEED measurements.

The induction periods observed in XPS measurements are clarified by the STM results, and the different stages of the reduction process are shown in Fig. 7a and b. In both cases, during exposure at room temperature and following the 500 K flash, the formation of defects, in the form of triangular dislocation loops, precedes the growth of the more reduced $p(3 \times 3)$ and $p(2 \times 2)$ phases. At room temperature, however, the formation of these defects is slow, and only occurs when a sufficient OH coverage is reached. We note that significant removal of oxygen from the surface only occurs during formation of the $p(2 \times 2)$ and $p(3 \times 3)$ structures, as the vacancy concentrations present in the form of dislocation loops (at the threshold density of 0.5 dislocation loops per unit cell) amount to only a few percent, and are therefore difficult to detect on the basis of O 1s intensities. The longer induction period observed in XPS measurements at room temperature thus corresponds directly to the difference in the onset of formation of the more reduced structures observed in STM and is limited exclusively by the initial rate of vacancy formation to produce the dislocation loops.

The combination of XPS and STM in our study adds further insight into the autocatalytic reduction mechanism originally proposed by Huang and Ranke. Vacancies created during the initial stage of reduction are stabilized in the form of dislocation loops and the formation of the $p(2 \times 2)$ structure does not start directly from single oxygen vacancies as a result of destabilized next-nearest O atoms along the O rows as they proposed [10]. As we have so far been unable to obtain well-resolved atomic scale STM images of the surface directly after H exposure, but before flashing to 500 K, we can not provide a precise mechanism for the reduction, which must involve restructuring of the Fe lattice in addition to removal

of oxygen. Nucleation and growth of the $p(2 \times 2)$ and $p(3 \times 3)$ structures appears to begin at the “pits” observed to form either at TOP* domains in the centers of larger dislocation loops or at TOP domains surrounded by three smaller dislocation loops (see, for example, Fig. 6c). This supports the notion that the presence of partially-reduced structures further facilitates the formation of more reduced structures. The reason for the rapid growth of these more reduced structures following the initial nucleation is still unclear, though we speculate that restructuring of the Fe lattice may be the limiting factor, and that the presumably greater flexibility of the more open Fe_3O_2 honeycomb lattice may further facilitate this transformation. If this is the case, the autocatalytic reaction observed for the purely two-dimensional FeO film may have little similarity to those observed on bulk-like iron oxides.

Fe atoms coordinated to two O atoms in a “linear” (neglecting coordinates normal to the surface) configuration are common to all the reduced FeO_x structures we have observed by STM. Reduction of the FeO film by atomic hydrogen can be described as a gradual progression from the stoichiometric FeO film, consisting entirely of 3-fold coordinated Fe atoms, to the dislocation loop structure, having $\sim 15\%$ 2-fold Fe atoms at half-saturation, to the $p(3 \times 3)$ Fe_4O_3 structure with 75% 2-fold Fe and finally to the $p(2 \times 2)$ Fe_3O_2 with 100% 2-fold Fe. The high stability of this $p(2 \times 2)$ Fe_3O_2 structure appears to prevent complete reduction to metallic Fe at room temperature.

Finally, we note the structural similarity between the Fe_3O_2 phase identified here and the structures of the Ti_2O_3 [1] and V_2O_3 [2] phases grown on Pt(1 1 1) and Pd(1 1 1), respectively, all of which consist of superpositions of honeycomb and kagomé lat-

tices. The Fe_3O_2 phase is unique in that the metal atoms, rather than the oxygen atoms, form the kagomé lattice. Given the current interest in highly-frustrated magnetic structures [37], the Fe_3O_2 film could be an interesting system for surface characterization by spin-sensitive techniques.

3.6. Water dissociation

Spectrum a2 in Fig. 8a shows the O 1s photoemission region of the Fe_3O_2 film after water exposure at room temperature at 1.0×10^{-6} mbar for 10 min. Comparison with the O 1s spectrum before exposure (spectrum a1) shows that a new peak develops at 531.6 eV, i.e. coincident with the observed binding energy for hydroxyl groups formed on the FeO film after exposure to atomic hydrogen. Simultaneously, we observe a small reduction in the FeO_x peak intensity, indicating that the water donates a proton to a neighboring O atom upon dissociation. Ideally we expect that the decrease in the FeO_x signal would be equal to half of the observed peak area due to hydroxyl groups. The measured ratio is 0.20, less than expected, suggesting that some of the donated hydrogen may be bound to Fe or Pt, or that a portion of the observed OH peak is due to molecularly adsorbed H_2O . The direct binding of a hydrogen atom to Fe seems plausible, based on the work of Parkinson et al. [38], which demonstrated the formation of HFeOH species upon reaction of Fe atoms with condensed water.

After flashing the hydroxylated Fe_3O_2 film to 500 K, we observe an O 1s spectrum (spectrum a3) which is indistinguishable from that observed before the water exposure, indicating that the hydroxyl groups formed upon water dosing leave the surface as H_2O once the surface is flashed to 500 K. In addition, the $p(2 \times 2)$

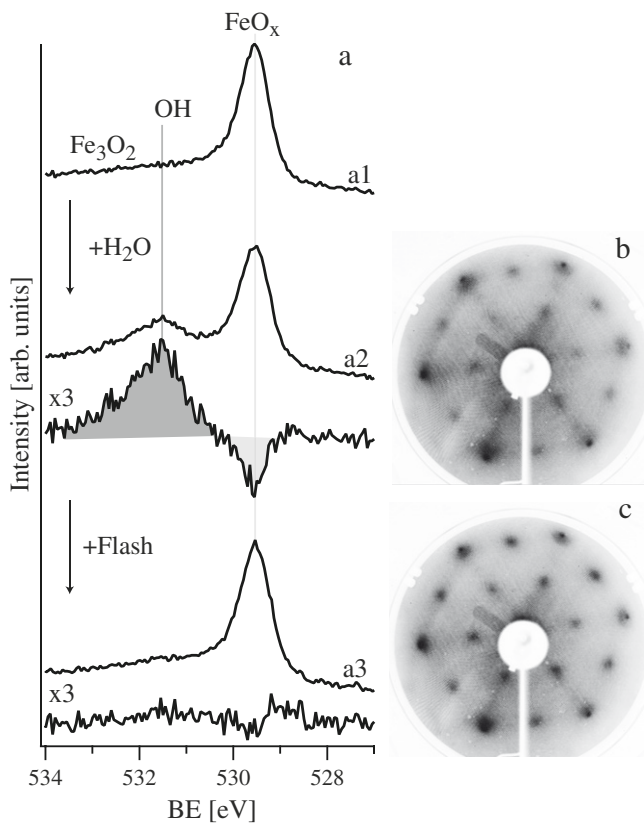


Fig. 8. (a) The O 1s region of the clean Fe_3O_2 phase (a1), after exposure to 600×10^{-6} mbar s H_2O at room temperature (a2), and after subsequently flashing to 500 K (a3). Magnified difference spectra referring to the Fe_3O_2 structure are shown below each spectrum. (b) 100.1 eV LEED image of the Fe_3O_2 structure after water exposure. (c) 100.1 eV LEED image of the water exposed and flashed Fe_3O_2 structure.

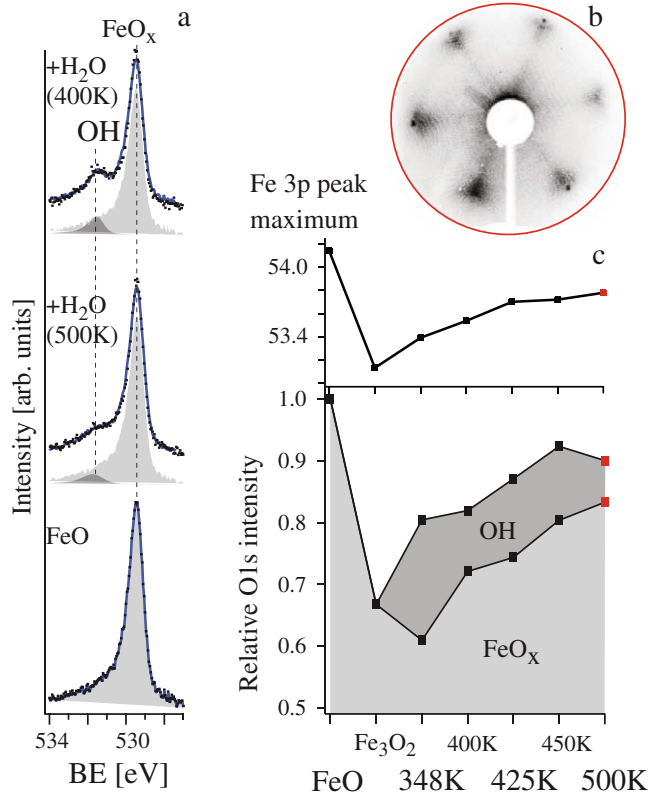


Fig. 9. (a) XP-spectra of the water-exposed Fe_3O_2 film taken after water exposure of 600×10^{-6} mbar s at different temperatures. The pristine FeO film is included for comparison. (b) 100.1 eV LEED image of the Fe_3O_2 film exposed to 600×10^{-6} mbar s of water at 500 K corresponding to the red points in c. (c) Coverage of FeO_x , OH and Fe 3p peak position calculated from the O 1s and Fe 3p spectra.

LEED pattern is weakened following water exposure (Fig. 8b), but regains its original intensity after heating to 500 K (Fig. 8c). We thus conclude that the water dissociation observed at room temperature is fully reversible.

Fig. 9a shows the O 1s spectra of the clean and the water-exposed Fe₃O₂ films for different exposure temperatures. Relative oxygen coverages deduced from these and similar plots are shown in Fig. 9c. The O 1s peak assigned to FeO_x increases with increasing temperature above 350 K while the peak characteristic of hydroxyl groups decreases. These two observations indicate that Fe₃O₂ film becomes re-oxidized by water exposure above 350 K. This conclusion is further supported by the increase in Fe 3p binding energy at higher dosing temperatures and the LEED pattern observed after water exposure at 500 K (see Fig. 9b). Here, the $p(2 \times 2)$ reflexes have disappeared and we start to observe a very weak rosette structure indicating that small FeO(1 1 1) domains are formed on the surface. Even though the Fe₃O₂ film clearly becomes re-oxidized when water is dosed above 350 K, it should be stressed that it was impossible to form the stoichiometric FeO film again under the experimentally tested temperature and pressure conditions.

Consistent with these XPS results, we observe with STM that a mildly-reduced FeO film, exhibiting dislocation loops, is unaffected by water exposure under high vacuum conditions. When water is dosed during measurement, however, we observe tip-induced dissociation of water at the dislocation loops inside the scanning area, while those outside are unaffected. The STM images shown in Fig. 10a are taken from an STM movie recorded in $\sim 2 \times 10^{-8}$ mbar H₂O and they clearly demonstrate that the dislocation loops can be removed completely by a stepwise reduction of their size. Consistent with water dissociation the stepwise size reduction suggests that one oxygen atom is added each time the size of the dislocation

loop shrinks as the model depicted in Fig. 10b shows. This effect is not observed for O₂, which does not dissociate at the dislocation loops at room temperature, even during STM measurements. Instead, we observe that the small quantities of water formed from O₂-induced desorption from the inner chamber walls [39] can re-oxidize the film during measurement. An example is depicted in Fig. 10c showing selected STM images from an STM movie recorded on the partly reduced FeO(1 1 1)/Pt(1 1 1) film in a background atmosphere of $\sim 1.3 \times 10^{-6}$ mbar O₂. Both dislocation loops (visible as dark lines and one of which is highlighted with a green triangle), and hydroxyls (imaged as yellow protrusions), are clearly visible in STM images. In the image taken after 15 s an additional bright double protrusion appears and the dimension of the adjacent dislocation loop shrinks by one lattice distance. After the bright double protrusion is formed, one of the hydroxyls diffuses to an adjacent lattice site and the two hydroxyls can easily be distinguished (image after 44 s). The fact that the double hydroxyl group appears exactly when the dislocation loop is observed to shrink by one FeO-lattice distance clearly demonstrates that the two hydroxyls are formed due to water dissociation in the pocket site located at the corner of the dislocation loop. A schematic of the most probable mechanism for water oxidation of the dislocation loops is depicted in Fig. 10d. The fact that the double hydroxyls are observed exclusively at the corner sites suggests that the barrier for dissociation is lower here than at the 2-fold coordinated Fe atoms located along the edges of the dislocation loops.

4. Conclusions

Using a combination of STM, XPS and DFT, we have studied the reduction by hydrogen of single-layer FeO films grown on Pt(1 1 1) by atomic hydrogen. We found that the reduction process starts with the development of triangularly shaped oxygen vacancy dislocation loops. More reduced $p(3 \times 3)$ (Fe₄O₃) and $p(2 \times 2)$ (Fe₃O₂) structures nucleate in the TOP domains once the oxygen lattice is reconstructed by the development of several oxygen vacancy dislocation loops in adjacent HCP domains. Structural models of all three reduced structures are proposed and as a general trend we find that the overall reduction process can be described as the gradual transformation of 3-fold oxygen-coordinated Fe atoms into 2-fold coordinated Fe atoms.

Furthermore, we have studied the interaction of water with the reduced iron-oxide films. In contrast to the inert FeO film, we find that the reduced structures are able to dissociate water. By heating the surface during water exposure, we find that the film can be partly re-oxidized.

Acknowledgments

We thank Karina Schulte, Joachim Schnadt and Jesper Andersen and the MAX-Lab staff for help with the XPS-experiments. The support to the iNANO center from the Danish Research Agency, the Strategic Research Council and the Danish Council for Independent Research is gratefully acknowledged as is the support from the Carlsberg and Villum Kahn Rasmussen Foundations, and the European Research Council. Work at UW was supported by DOE-BES, Chemical Sciences Division. Supercomputing time was utilized at NERSC, PNNL, and ORNL.

References

- [1] G. Barcaro, S. Agnoli, F. Sedona, G.A. Rizzi, A. Fortunelli, G. Granozzi, *J. Phys. Chem. C* 113 (2009) 5721.
- [2] S. Surnev, G. Kresse, M. Sock, M.G. Ramsey, F.P. Netzer, *Surf. Sci.* 495 (2001) 91.
- [3] F.P. Netzer, *Surf. Rev. Lett.* 9 (2002) 1553.
- [4] X.S. Liu, O. Korotkikh, R. Farrauto, *Appl. Catal. A* 226 (2002) 293.
- [5] M. Watanabe, H. Uchida, K. Ohkubo, H. Igarashi, *Appl. Catal. B* 46 (2003) 595.

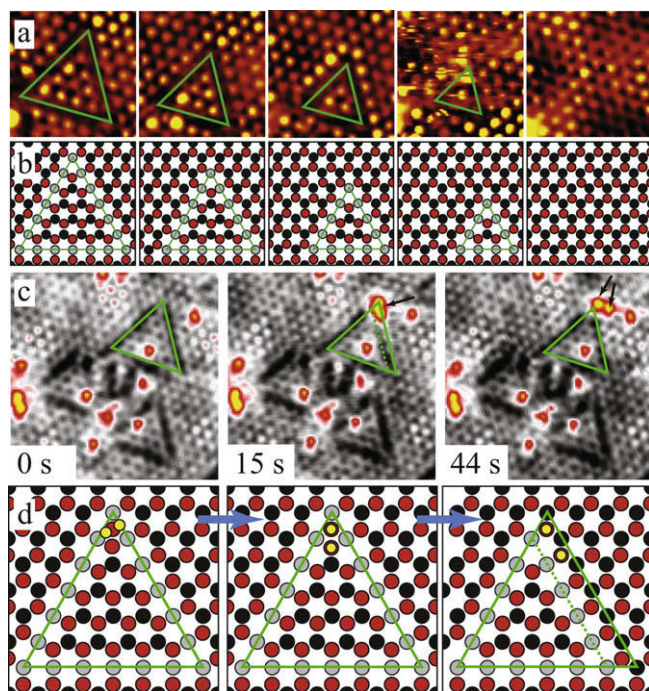


Fig. 10. (a) STM images taken from an STM movie recorded in 2×10^{-8} mbar H₂O. (b) Model showing the stepwise size reduction of the dislocation loops. (c) STM images from an STM movie taken in 6.6×10^{-6} mbar O₂. Notice that the dislocation loop shrinks (indicated by green triangles) simultaneously with the development of double hydroxyl groups. Finally the hydrogen atoms diffuse away from each other. (d) Model of the water dissociation in the pocket sites formed by the corners of the dislocation loops. (For interpretation of the references to colour in this figure legend, the reader is referred to the web version of this article.)

- [6] T. Toda, H. Igarashi, H. Uchida, M. Watanabe, *J. Electrochem. Soc.* 146 (1999) 3750.
- [7] T. Healey, P.D. Devries, Patent, WO2007019361-A1, US2007183968-A1, EP1919823-A1, 2007.
- [8] A. Basinska, T.P. Maniecki, W.K. Jozwiak, *React. Kinet. Catal. Lett.* 89 (2006) 319.
- [9] Z.H. Qin, M. Lewandowski, Y.N. Sun, S. Shaikhutdinov, H.J. Freund, *J. Phys. Chem. C* 112 (2008) 10209.
- [10] W.X. Huang, W. Ranke, *Surf. Sci.* 600 (2006) 793.
- [11] C. Wang, H. Daimon, S.H. Sun, *Nano Lett.* 9 (2009) 1493.
- [12] Y.N. Sun, Z.H. Qin, M. Lewandowski, E. Carrasco, M. Sterrer, S. Shaikhutdinov, H.J. Freund, *J. Catal.* 266 (2009) 359.
- [13] H.C. Galloway, J.J. Benitez, M. Salmeron, *Surf. Sci.* 298 (1993) 127.
- [14] W. Ranke, M. Ritter, W. Weiss, *Phys. Rev. B* 60 (1999) 1527.
- [15] Y.J. Kim, C. Westphal, R.X. Ynzunza, H.C. Galloway, M. Salmeron, M.A. VanHove, C.S. Fadley, *Phys. Rev. B* 55 (1997) 13448.
- [16] L.R. Merte, J. Knudsen, L.C. Grabow, R.T. Vang, E. Laegsgaard, M. Mavrikakis, F. Besenbacher, *Surf. Sci.* 603 (2009) L15.
- [17] U. Leist, W. Ranke, K. Al-Shamery, *Phys. Chem. Chem. Phys.* 5 (2003) 2435.
- [18] Y. Joseph, C. Kuhrs, W. Ranke, M. Ritter, W. Weiss, *Chem. Phys. Lett.* 314 (1999) 195.
- [19] E. Laegsgaard, F. Besenbacher, K. Mortensen, I. Stensgaard, *J. Microsc.-Oxford* 152 (1988) 663.
- [20] W.X. Huang, W. Ranke, R. Schlogl, *J. Phys. Chem. C* 111 (2007) 2198.
- [21] R. Nyholm, J.N. Andersen, U. Johansson, B.N. Jensen, I. Lindau, *Nucl. Instrum. Methods Phys. Res. A* 467 (2001) 520.
- [22] G.H. Vurens, M. Salmeron, G.A. Somorjai, *Surf. Sci.* 201 (1988) 129.
- [23] S.L. Dudarev, G.A. Botton, S.Y. Savrasov, C.J. Humphreys, A.P. Sutton, *Phys. Rev. B* 57 (1998) 1505.
- [24] L. Giordano, G. Pacchioni, J. Goniakowski, N. Nilius, E.D.L. Rienks, H.J. Freund, *Phys. Rev. B* 76 (2007) 075416.
- [25] G. Kresse, J. Hafner, *Phys. Rev. B* 47 (1993) 558.
- [26] G. Kresse, J. Furthmuller, *Phys. Rev. B* 54 (1996) 11169.
- [27] J.P. Perdew, J.A. Chevary, S.H. Vosko, K.A. Jackson, M.R. Pederson, D.J. Singh, C. Fiolhais, *Phys. Rev. B* 46 (1992) 6671.
- [28] W.A. Hofer, A.S. Foster, A.L. Shluger, *Rev. Mod. Phys.* 75 (2003) 1287.
- [29] M. Schmid, H. Stadler, P. Varga, *Phys. Rev. Lett.* 70 (1993) 1441.
- [30] L. Ruan, F. Besenbacher, I. Stensgaard, E. Laegsgaard, *Phys. Rev. Lett.* 70 (1993) 4079.
- [31] G.O. Potschke, R.J. Behm, *Phys. Rev. B* 44 (1991) 1442.
- [32] P. Liu, T. Kendelewicz, G.E. Brown, E.J. Nelson, S.A. Chambers, *Surf. Sci.* 417 (1998) 53.
- [33] Y. Joseph, W. Ranke, W. Weiss, *J. Phys. Chem. B* 104 (2000) 3224.
- [34] F. Sirotti, G. Rossi, *Phys. Rev. B* 49 (1994) 15682.
- [35] S. Wendt et al., *Surf. Sci.* 598 (2005) 226.
- [36] T. Mitsui, E. Fomin, D.F. Ogletree, M. Salmeron, A.U. Nilekar, M. Mavrikakis, *Angew. Chem. Int. Ed. Engl.* 46 (2007) 5757.
- [37] J.E. Greedan, *J. Mater. Chem.* 11 (2001) 37.
- [38] G.S. Parkinson, Y.K. Kim, Z. Dohnalek, R.S. Smith, B.D. Kay, *J. Phys. Chem. C* 113 (2009) 4960.
- [39] J. Matthiesen et al., *ACS Nano* 3 (2009) 517.